

Electric welding arc modeling with the solver OpenFOAM

- A comparison of different electromagnetic models -

Isabelle Choquet¹, Alireza Javidi Shirvan¹, Håkan Nilsson²

¹University West, Department of Engineering Science, Trollhättan, Sweden,

²Chalmers University of Technology, Department of Applied Mechanics, Gothenburg, Sweden
isabelle.choquet@hv.se

ABSTRACT

This study focuses on the modeling of a plasma arc heat source in the context of electric arc welding. The model was implemented in the open source CFD software OpenFOAM-1.6.x, coupling thermal fluid mechanics in three dimensions with electromagnetics. Four different approaches were considered for modeling the electromagnetic fields: i) the three-dimensional approach, ii) the two-dimensional axi-symmetric approach, iii) the electric potential formulation, and iv) the magnetic field formulation as described by Ramírez *et al.* [1]. The underlying assumptions and the differences between these models are described in detail. Models i) to iii) reduce to the same quasi one-dimensional limit for an axi-symmetric configuration with negligible radial current density, contrary to model iv). Models ii) to iv) do not represent the same physics when the radial current density is significant, such as or an electrode with a conical tip. Models i) to iii) were retained for the numerical simulations. The corresponding results were validated against the analytic solution of an infinite electric rod. Perfect agreement was obtained for all the models tested. The results from the coupled solver (thermal fluid mechanics coupled with electromagnetics) were compared with experimental measurements for Gas Tungsten Arc Welding (GTAW). The shielding gas was argon, the arc was short (2mm), the electrode tip was conical, and the configuration was axi-symmetric. The boundary conditions were specified at the anode and cathode surfaces. Models i) and ii) lead to the same results, but not the model iii). Model iii) neglects the radial current density component, resulting in a poor estimation of the magnetic field, and in turn of the arc fluid velocity. The limitations of the coupled solver were investigated changing the gas composition, and using different boundary conditions. The boundary conditions, difficult to measure and to estimate a priori, significantly affect the simulation results.

Keywords: electric arc welding, thermal plasma, short arc, electromagnetic model, electric potential formulation, magnetic field formulation, GTAW.

1 INTRODUCTION

The first man made electric arc was produced in 1800 by Sir Humphry Davy using carbon electrodes. Electric arc welding as a method of assembling metal parts through fusion was however initiated much later,

at the end of the 19's century, when C.L. Coffin introduced the metal electrode and the metal transfer across an arc. Thanks to intense developments in the early 1900's, such as the first coated electrode developed by A.P. Strohmenger and O. Kjellberg, electric arc welding started being utilized in production in the

1920's, and then in large scale production from the 1930's.

This manufacturing process, although used since many decades, is still under intensive development, in order to further improve different aspects such as process productivity, process control, and weld quality. Such improvements are beneficial both from economical and environmental sustainability.

Electric arc welding is interdisciplinary in nature, and complex to master as it involves very large temperature gradients, and a number of parameters that do interact in a non-linear way. Its investigation was long based on experimental studies. Today, thanks to recent and significant progress done in the field of welding simulation, experiments can be complemented with numerical modeling to reach a deeper process understanding. As an illustration, the change in microstructure can be simulated for a given thermal history within the heat affected zone of the base metal, as shown in [2]. Numerical calculations of the residual stresses, to investigate fatigue and distortion, can now be coupled with the weld pool as in [3], calibrating functional approximations of volume and surface heat flux transferred from the electric arc.

Electric arcs used in welding are generally coupling an electric discharge between an anode and a cathode, with a shielding gas flow. The main goal is to form a shielding gas flow with a temperature large enough to melt the materials to be welded, i.e. a thermal plasma flow. The numerical modeling of thermal plasma flow is thus a key element for characterizing the thermal history of an electric arc welding process. It determines the thermal energy provided to the parent metal, its spatial distribution, and also the pressure force applied by the arc on the weld pool.

A thermal plasma is basically modeled coupling thermal fluid mechanics (governing mass, momentum and energy or enthalpy) with electromagnetics (governing the electric field, the magnetic field, and the current density). Different thermal plasma models can be found in the literature in the context of electric arc simulation. The first model coupling thermal fluid mechanics and electromagnetics to simulate an axisymmetric high-intensity free burning arc was developed by Hsu *et al.* in 1983, and applied to a 10 mm long arc [4]. Since then many developments have been done to address in more detail various aspects of the electric arc heat source. Within the frame of axi-

symmetric configurations, Tanaka *et al.* accounted for chemical non-equilibrium [5]. Yamamoto *et al.* investigated the influence of metal vapor on the properties of a plasma arc [6]. Wendelstorf coupled arc, anode and cathode including the plasma sheath [7]. Tanaka *et al.* and Hu *et al.* coupled arc and weld pool accounting for melting [8], [9]. Some of these models have also been extended to three space-dimensions by Xu *et al.* for instance [10]. These studies are based on the same thermal fluid model (up to the space dimension) for describing the core of the plasma arc. However, various models are used for determining the electromagnetic fields. Among them are the three-dimensional formulation with magnetic potential, Gonzales *et al.* [11], or with magnetic field, Xu *et al.* [10]. In the context of axisymmetric applications few authors use the magnetic field formulation introduced by McKelliget and Szekely [14]. Few authors, such as Lago *et al.* [12], Bini *et al.* [13], use instead a two-dimensional axisymmetric model (combining the magnetic field formulation with a Poisson equation for governing the electric potential). The electric potential formulation introduced by Hsu *et al.* [4] is retained by many authors. The electric potential formulation and the magnetic field formulation, developed for two-dimensional axisymmetric configurations, were initially applied to rather long arcs without accounting for the geometry of the electrode tip. These formulations have been compared by Ramírez *et al.* [1] for arc lengths of 6.3 and 10 mm. It is often considered that these formulations do represent the same physics. When tested numerically, it is however observed that they do lead to results presenting some differences. These differences are usually considered to be due to mathematical and numerical issues, as underlined by Ramírez *et al.*, [1].

The aim of the present study is to develop a simulation tool for thermal plasma arc applied to electric arc welding, and thus to short arcs. The implementation was done in the open source CFD software OpenFOAM-1.6.x (www.openfoam.com), considering three space dimensions. OpenFOAM was distributed as OpenSource in 2004. This simulation software is a C++ library of object-oriented classes that can be used for implementing solvers for continuum mechanics. It includes a number of solvers for different continuum mechanical problems. Due to the availability of the source code, its libraries can be used to implement new solvers for other applications. The current

implementation is based on the buoyantSimpleFoam solver, which is a steady-state solver for buoyant, turbulent flow of compressible fluids. The partial differential equations of this solver are discretized using the finite volume method.

The thermal plasma simulation model implemented in the present work is described in section 2. It couples a system of thermal Navier-Stokes equations in three space-dimensions (section 2.1) with a simplified system of Maxwell equations (section 2.2). Different simplifications were considered for modeling the electromagnetic fields:

- i) the three-dimensional approach,
- ii) the two-dimensional axi-symmetric approach,
- iii) the quasi one-dimensional approach,
- iv) the electric potential formulation, and
- v) the magnetic field formulation.

The underlying assumptions and the differences between these models are detailed in section 2.2.

Models i), ii) and iv) were retained for doing numerical tests. The electromagnetic part of the solver was tested against the analytic solution of an infinite electric rod. The test case and the results are presented in section 3.1.

The coupled solver was tested against experimental measurements for Gas Tungsten Arc Welding (GTAW) done by Haddad and Farmer [15]. That case was also used by Tsai and Sindo Kou [16] for modeling and simulating welding arcs produced by sharpened and flat electrodes. The shielding of the test case gas is argon, the experimental configuration is axi-symmetric, and the arc length (2 mm) is not long compared to the electrode tip radius (0.5 mm). The anode and cathode were treated as boundary conditions in the simulations, accounting for the geometry of the electrode tip. This second test case, and the related simulation results, are presented in section 3.2. For each test case the approaches i), ii) and iv) were used for calculating the magnetic field, and their validity discussed.

The limitations of the coupled solver were also investigated changing the gas composition, and testing various boundary conditions on the anode and cathode to evaluate their influence on the plasma arc. The corresponding simulation results are presented and discussed in sections 3.3 and 3.4. The main results and conclusions are summarized in section 4.

2 MODEL

The model described in the present work was retained as first step in the development of a simulation tool for thermal plasma arc applied to electric arc welding. The implementation was done in the continuation of the work done by Sass-Tisovskaya [17]. The implementation was done in the open source CFD software OpenFOAM-1.6.x (www.openfoam.com), coupling thermal fluid mechanics with electromagnetics. The fluid and electromagnetic models are tightly coupled. The Lorentz force, or magnetic pinch force, resulting from the induced magnetic field indeed acts as the main cause of plasma flow acceleration. The Joule heating due to the electric field is the largest heat source governing the plasma energy (and thus temperature). On the other hand the system of equations governing electromagnetics is temperature dependent, via the electric conductivity. The main details of the implemented thermal fluid and electromagnetic models are described in the following sections.

2.1 Thermal fluid model

The thermal fluid part of the model was derived by Choquet and Lucquin-Desreux [18] from a system of Boltzmann type transport equations using kinetic theory. A viscous hydrodynamic/diffusion limit was obtained in two stages doing a Hilbert expansion and using the Chapman-Enskog method. The resultant viscous fluid model is characterized by two temperatures, and non equilibrium ionization. It applies to the arc plasma core and the ionization zone of the arc plasma sheath. The model implemented here is a simplified version of that model neglecting the arc plasma sheath. The thermal fluid component of the model applies to a Newtonian and thermally expansible fluid, assuming:

- a one-fluid model,
- in local thermal equilibrium,
- mechanically incompressible, because of the small Mach number, and
- a steady-state and laminar flow.

The model is thus suited to the plasma core. In this framework the continuity equation is written as

$$\nabla \cdot [\rho(T) \vec{u}] = 0, \quad (1)$$

where ρ denotes the fluid density, \vec{u} the fluid velocity, and $\nabla \cdot$ the divergence operator. The density $\rho = \rho(T)$ depends here on the temperature T , as illustrated for argon plasma in Fig. 1.

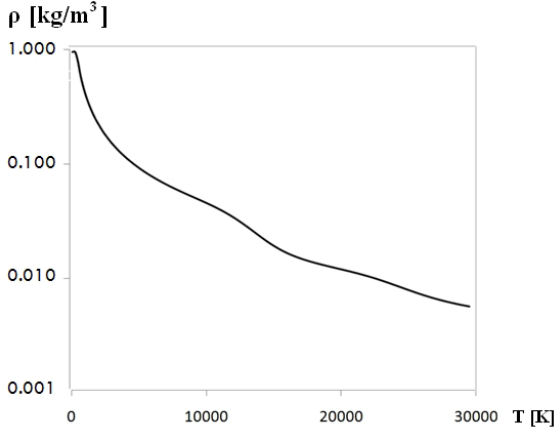


Figure 1: Argon plasma density as a function of temperature.

The momentum conservation equation is expressed as

$$\begin{aligned} \nabla \cdot [\rho(T) \vec{u} \otimes \vec{u}] - \vec{u} \nabla \cdot [\rho(T) \vec{u}] \\ - \nabla \cdot [\mu(T) (\nabla \vec{u} + (\nabla \vec{u})^T) - \frac{2}{3} \mu(T) (\nabla \cdot \vec{u}) I] \quad (2) \\ = -\nabla P + \vec{J} \times \vec{B}, \end{aligned}$$

where μ the viscosity, I is the identity tensor, P the pressure, \vec{B} the magnetic flux density (simply called magnetic field in the sequel), \vec{J} the current density, ∇ denotes the gradient operator, \otimes and \times the tensorial and vectorial product, respectively. The last term on the right hand side of Eq. (2) is the Lorentz force.

The enthalpy conservation equation is

$$\begin{aligned} \nabla \cdot [\rho(T) \vec{u} h] - h \nabla \cdot [\rho(T) \vec{u}] - \nabla \cdot [\alpha(T) \nabla h] \\ = \nabla \cdot (\vec{u} P) - P \nabla \cdot \vec{u} + \vec{J} \cdot \vec{E} \\ - Q_{rad} + \nabla \cdot \left[\frac{5 k_B \vec{J}}{2 e C_p(T)} h \right], \quad (3) \end{aligned}$$

where h is the specific enthalpy, α is the thermal diffusivity, \vec{E} the electric field, Q_{rad} the radiation heat loss [19], k_B the Boltzmann constant, e the elementary charge, and C_p the specific heat at constant pressure.

The third term on the right hand side of Eq. (3) is the Joule heating, and the last term the transport of electron enthalpy. The temperature, T , is derived from the specific enthalpy via the definition of the specific heat,

$$C_p(T) = \left(\frac{dh}{dT} \right)_P, \quad (4)$$

which is plotted in Fig. 2 for Ar and CO₂ plasma.

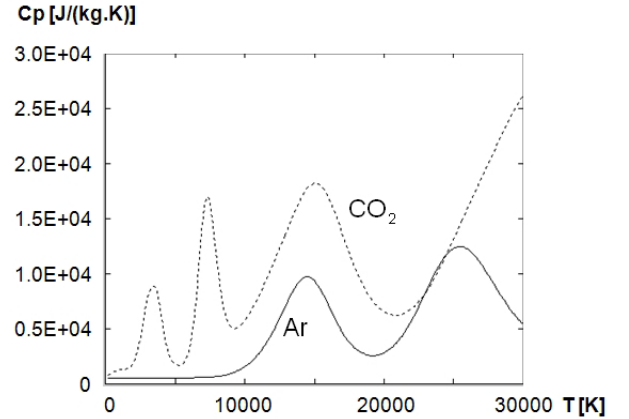


Figure 2: Specific heat as a function of temperature for Ar (solid line) and CO₂ (dotted line).

The thermodynamic and transport properties are linearly interpolated from tabulated data implemented on a temperature range from 200 to 30 000 K, with a temperature increment of 100 K. These data tables were derived for argon plasma [20], and carbon dioxide plasma [21], using kinetic theory.

2.2 Electromagnetic models

As mentioned in the introduction, different approaches can be found in the literature devoted to the simulation of electric arcs for calculating the electromagnetic source terms of Eqs. (2)-(3): the three-dimensional approach, the two-dimensional axi-symmetric approach, the electric potential formulation, and the magnetic field formulation (we here refer to the version described by Ramírez *et al.* [1]). These approaches and formulations are recalled below, as well as the quasi 1-dimensional case, in order to discuss the underlying assumptions. All of them are derived from the following set of Maxwell equations:

Gauss' law for magnetism

$$\nabla \cdot \vec{B} = 0, \quad (5)$$

Gauss' law

$$\nabla \cdot \vec{E} = \epsilon_o^{-1} q_{tot}, \quad (6)$$

Faraday's law

$$\frac{\partial \vec{B}}{\partial t} = -\nabla \times \vec{E}, \quad (7)$$

and, Ampère's law

$$\epsilon_o \mu_o \frac{\partial \vec{E}}{\partial t} = \nabla \times \vec{B} - \mu_o \vec{J}, \quad (8)$$

where q_{tot} is the total electric charge per unit volume, ϵ_o the permittivity of vacuum, μ_o the permeability of vacuum, and $\nabla \times$ denotes the rotational operator.

The Maxwell equations are supplemented by the equation governing charge conservation

$$\frac{\partial q_{tot}}{\partial t} + \nabla \cdot \vec{J} = 0, \quad (9)$$

and the generalized Ohm law

$$\vec{J} = \vec{J}_{drift} + \vec{J}_{ind} + \vec{J}_{Hall} + \vec{J}_{diff} + \vec{J}_{ther}, \quad (10)$$

where $\vec{J}_{drift} = \sigma \vec{E}$ denotes the conduction current due to electron drift, σ the electric conductivity, \vec{J}_{ind} the induction current due to the induced magnetic field \vec{B} , \vec{J}_{Hall} the Hall current resulting from the electric field induced by \vec{B} , \vec{J}_{diff} the diffusion current due to electron pressure gradients, and \vec{J}_{ther} the thermodiffusion current due to gradients in electron temperature. The electric conductivity $\sigma = \sigma(T)$ is here temperature dependent, as illustrated in Fig. 3 for an argon plasma. In the frame of electric arcs applied to welding, and when considering the plasma core (and not the plasma sheaths), it can be assumed that

A1- The Debye length λ_D is much smaller than the characteristic length of the welding arc, so that local electro-neutrality is verified, $q_{tot} = 0$, and the diffusion and thermodiffusion currents due to electrons are small compared to the drift current.

A2- The characteristic time and length of the welding arc allow neglecting the displacement current $\mu_o \partial \vec{E} / \partial t$

compared to the current density \vec{J} in Ampère's law, resulting in quasi-steady electromagnetic phenomena, $\partial \vec{E} / \partial t = 0$, and $\partial \vec{B} / \partial t = 0$.

A3- The Larmor frequency is much smaller than the average collision frequency of electrons, implying a negligible Hall current compared to the drift current.

A4- The magnetic Reynolds number is much smaller than unity, leading to a negligible induction current compared to the drift current.

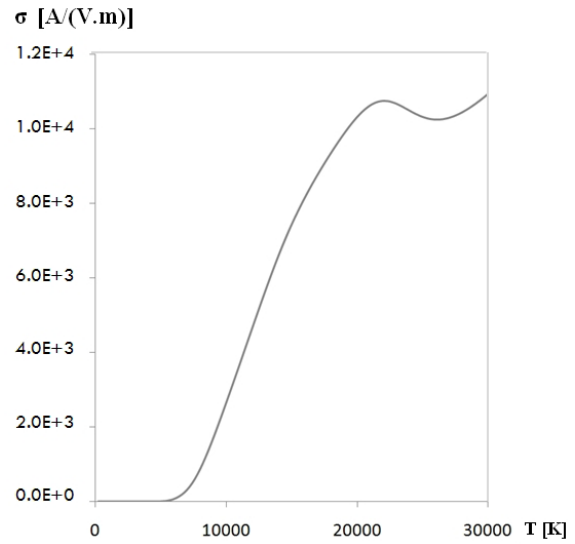


Figure 3: Argon plasma electric conductivity as a function of temperature.

Based on these assumptions, Eqs. (5)-(10) do respectively reduce to

$$\nabla \cdot \vec{B} = 0, \quad (11)$$

$$\nabla \cdot \vec{E} = 0, \quad (12)$$

$$\nabla \times \vec{E} = \vec{0}, \quad (13)$$

$$\nabla \times \vec{B} = \mu_o \vec{J}, \quad (14)$$

$$\nabla \cdot \vec{J} = 0, \quad (15)$$

and

$$\vec{J} = \sigma(T) \vec{E}. \quad (16)$$

The set of equations (11)-(16) are usually combined in the following more convenient form. As the electric field \vec{E} is irrotational (from Eq. (13)), as the magnetic field \vec{B} is of constant zero divergence (from Eq. (11)), and electromagnetic phenomena can be assumed quasi-steady (assumption A2), there exist a scalar electric potential V and a vector magnetic potential \vec{A} defined up to a constant such that,

$$\vec{E} = -\nabla V, \quad (17)$$

and

$$\vec{B} = \nabla \times \vec{A}. \quad (18)$$

Using these properties, Eqs. (15) and (16) lead to the Poisson scalar equation governing the electric potential

$$\nabla \cdot [\sigma(T) \nabla V] = 0. \quad (19)$$

The remaining equation (14) leads to the vector equation governing the magnetic potential,

$$\nabla \times \nabla \times \vec{A} = \nabla \cdot (\nabla \vec{A}) - \Delta \vec{A} = \mu_o \vec{J}, \quad (20)$$

where Δ denotes the Laplace operator.

An additional condition then needs to be imposed in order to uniquely define \vec{A} and V . This condition is given here by the Lorentz gauge, $\nabla \cdot \vec{A} = 0$. Then, using Eqs. (16) and (17), the equation governing the magnetic potential \vec{A} reduces to the Poisson vector equation

$$\Delta \vec{A} = \mu_o \sigma(T) \nabla V. \quad (21)$$

2.2.1 Three-dimensional approach

When considering a three-dimensional approach the electromagnetic model for a welding arc plasma core uses Eqs. (19) and (21). The electric field \vec{E} , the electric current \vec{J} and the magnetic field \vec{B} entering the source terms of the fluid set of equations (section 2.1) are derived from V and \vec{A} through Eqs. (17), (16), and (18), respectively.

It should be noticed that the model used by Xu *et al.* [10] is the same, although these authors did not introduce explicitly the magnetic potential.

2.2.2 Two-dimensional axi-symmetric approach

Here, the particular case of an axi-symmetric configuration is considered, such as water cooled cathode TIG welding. A cylindrical coordinate system (r, θ, z) is then introduced. Additional simplifications can now be done thanks to the invariance by rotation about the symmetry axis. It results in no gradient along the azimuthal direction θ , a current density $\vec{J}(r, z) = (J_r(r, z), 0, J_z(r, z))$ with a constant zero angular component $J_\theta = 0$, and a magnetic field $\vec{B}(r, z) = (0, B_\theta(r, z), 0)$ along the azimuthal direction. Then the electromagnetic model of section 2.2.1 simplifies to the Poisson equation governing the electric potential $V(r, z)$

$$\frac{1}{r} \frac{\partial}{\partial r} \left(r \sigma(T) \frac{\partial V}{\partial r} \right) + \frac{\partial}{\partial z} \left(\sigma(T) \frac{\partial V}{\partial z} \right) = 0, \quad (22)$$

and two scalar Poisson equations governing the magnetic potential $\vec{A}(r, z) = (A_r(r, z), 0, A_z(r, z))$

$$\frac{1}{r} \frac{\partial}{\partial r} \left(r \frac{\partial A_r}{\partial r} \right) + \frac{\partial^2 A_r}{\partial z^2} - \frac{A_r}{r^2} = \mu_o \sigma(T) \frac{\partial V}{\partial r}, \quad (23)$$

and

$$\frac{1}{r} \frac{\partial}{\partial r} \left(r \frac{\partial A_z}{\partial r} \right) + \frac{\partial^2 A_z}{\partial z^2} = \mu_o \sigma(T) \frac{\partial V}{\partial z}. \quad (24)$$

Using the Lorentz gauge

$$\frac{1}{r} \frac{\partial(rA_r)}{\partial r} + \frac{\partial A_z}{\partial z} = 0, \quad (25)$$

and the definition of the magnetic potential, Eq. (18), we can easily see that Eqs. (23)-(24) also write

$$\frac{\partial B_\theta}{\partial z} = \mu_o \sigma(T) \frac{\partial V}{\partial r} = -\mu_o J_r, \quad (26)$$

and

$$\frac{1}{r} \frac{\partial(rB_\theta)}{\partial r} = -\mu_o \sigma(T) \frac{\partial V}{\partial z} = \mu_o J_z, \quad (27)$$

which is the Gauss law in cylindrical coordinates and in the particular case of an axi-symmetric problem. Eqs. (26)-(27) can be condensed into a single relation, for which two options are possible. The first option leads to a partial differential equation and the second to an integral relation defining B_θ . The partial differential formulation

$$\frac{\partial}{\partial r} \left(\frac{1}{\sigma r} \frac{\partial(rB_\theta)}{\partial r} \right) + \frac{\partial}{\partial z} \left(\frac{1}{\sigma} \frac{\partial B_\theta}{\partial z} \right) = 0, \quad (28)$$

is easily derived from Eqs. (26)-(27) as $\partial^2 V/(\partial r \partial z) = \partial^2 V/(\partial z \partial r)$. It should be noticed that Eq. (28) is the induction diffusion equation involved in the magnetic field formulation.

The integral formulation is also derived from Eqs. (26)-(27), using now the fact that $\partial^2 B_\theta/(\partial r \partial z) = \partial^2 B_\theta/(\partial z \partial r)$, so that

$$\frac{1}{r} \frac{\partial B_\theta}{\partial z} = \mu_o \left(\frac{\partial J_r}{\partial r} + \frac{\partial J_z}{\partial z} \right), \quad (29)$$

and thus

$$\begin{aligned} B_\theta(r, z) - B_\theta(r, z_o) \\ = r \mu_o \int_{l=z_o}^{l=z} \left(\frac{\partial J_z}{\partial z} + \frac{\partial J_r}{\partial r} \right)(r, l) dl. \end{aligned} \quad (30)$$

This integral relation defining the azimuthal component of the magnetic field can be further simplified to

$$B_\theta(r, z) = -\mu_o \int_{l=z_o}^{l=z} J_r(r, l) dl + B_\theta(r, z_o), \quad (31)$$

using the Poisson equation (22) and the relations

$$J_r(r, z) = \sigma(T) E_r(r, z) = -\sigma(T) \frac{\partial V}{\partial r}, \quad (32)$$

and

$$J_z(r, z) = \sigma(T) E_z(r, z) = -\sigma(T) \frac{\partial V}{\partial z}, \quad (33)$$

resulting from Eqs. (16) and (17).

To summarize, when considering a two-dimensional axi-symmetric approach the electromagnetic model for a welding arc plasma core is made of three scalar equations or less depending on the formulation retained for deriving the magnetic field. These equations include:

- the scalar Poisson equation, Eq. (22), governing the electric potential V , supplemented by the Eqs. (32) and (33) for deriving the electric field and the current density, and

- either B1, B2 or B3 for deriving the azimuthal component of the magnetic field:

B1 - The two scalar Poisson equations, Eqs. (23)-(24), governing the non-zero components of the magnetic potential \vec{A} , supplemented by Eq. (18) yielding

$$B_\theta(r, z) = \frac{\partial A_r}{\partial z} - \frac{\partial A_z}{\partial r}. \quad (34)$$

B2- The scalar induction diffusion equation, Eq. (28).

B3- The integral relation, Eq. (31).

B1 to B3 are based on the same assumptions. Formulation B3 seems to be the simplest one, with only one integral relation and no additional partial differential equation to solve. However it requires setting the reference value for the magnetic field, $B_\theta(r, z_o)$ at some well chosen location z_o , which is a difficulty. Also, integrating the current along the axial direction may require a careful implementation work when accounting for electrode tip angle (the cells of the mesh may not be everywhere aligned along the axial direction). B2 may thus be easier to implement if the interior of the anode and cathode is included in the computational domain, since then the magnetic field can easily be set on the boundaries of the computational domain. However if, as in the present study, only the surface of the anode and cathode is accounted for (as boundary of the computational domain), the specification of the magnetic field on the boundaries may turn out to be difficult too. In that case formulation B1 based on the magnetic potential is indeed more convenient, and thus retained for the simulation tests of section 3. Notice that formulation B1 was also used by Lago *et al.* [12] and Bini *et al.* [13] for instance.

2.2.3 Quasi one-dimensional approach

Here a simpler axi-symmetric case is considered, assuming in addition a negligible radial current density. The current density vector is thus aligned with the direction of the symmetry axis, $\vec{J}(r) = (0, 0, J_z(r))$, and the magnetic field is azimuthal with $\vec{B}(r) = (0, B_\theta(r), 0)$. The scalar Poisson equation governing the electric potential, Eq. (22), now further simplifies to

$$\frac{\partial}{\partial z} \left(\sigma(T) \frac{\partial V}{\partial z} \right) = 0, \quad (35)$$

with the remaining vector component

$$J_z = \sigma(T) E_z = -\sigma(T) \frac{\partial V}{\partial z}. \quad (36)$$

Eqs. (26)-(27) reduce to

$$\frac{1}{r} \frac{\partial (r B_\theta)}{\partial r} = \mu_o J_z, \quad (37)$$

so that the magnetic field can be defined by the following well-known integral relation

$$B_{\theta}(r) = \frac{\mu_0}{r} \int_{l=r_0}^{l=r} l J_z(l) dl + B_{\theta}(r_0) . \quad (38)$$

The reference value $B_{\theta}(r_0)$ can easily be set to zero taking the symmetry axis as reference location ($r_0 = 0$).

The electric potential formulation and the magnetic field formulation, which are more commonly used than the axi-symmetric approach of section 2.2.2 and the quasi one-dimensional approach of section 2.2.3, are recalled below. Each of these formulations is a simplified version of the axi-symmetric approach. The simplifications have the advantage of further reducing the electromagnetic model down to a single partial differential equation.

2.2.4 The electric potential formulation

The electric potential formulation, detailed in [4], combines two different levels of modeling:

- a two-dimensional axi-symmetric approach for defining the electric potential, Eq. (22), the current density and the electric field, Eqs. (32)-(33), with
- a quasi one-dimensional approach for defining the magnetic field, Eq. (38).

It should be noticed that in the limit of a negligible radial current density compared to the axial current density, the electric potential formulation reduces to the quasi one-dimensional formulation (section 2.2.3).

The electric potential formulation was initially applied to long arcs, i.e. arcs with a distance between anode and cathode rather large compared to the electrode radius. In addition it was applied, such as in the work by Hsu *et al.* [4] and Ramirez *et al.* [1], considering the domain below the electrode and not next to it. Also the boundary conditions set were those of an infinite electric rod. In this framework the radial current density component is less than the axial current density component, so that the quasi one-dimensional approach for the magnetic field is a good approximation.

The electric potential formulation is known to be accurate for predicting the arc temperature for axi-symmetric configurations [1]. This is indeed due to the fact that the axi-symmetric formulation (section 2.2.2) and the electric potential formulation are based

on the same assumptions for defining the electric potential. However, the electric potential formulation is also known to be less accurate for calculating the arc velocity [1]. This is due to the simplification done when evaluating the magnetic field. This lower accuracy, almost negligible for long arcs, is thus expected to be more significant when two-dimensional effects become more important, i.e. for short arcs, and/or when considering the geometry of the electrode tip (such as a tip angle).

2.2.5 The magnetic field formulation

The magnetic field formulation, introduced by McKelliget and Szekely [14], is derived from the axi-symmetric approach alone. As underlined by Ramirez *et al.* [1], an advantage of this formulation is to allow deriving the current density from the azimuthal component of the magnetic field without the need to solve the electric potential or the electric field. This formulation is indeed made of

- the induction diffusion equation, Eq. (28), for defining the magnetic field, from which the current density is directly derived using Eqs. (26)-(27).

Contrary to the electric potential formulation, the magnetic formulation is known to be accurate for predicting the arc velocity, but less accurate for calculating the arc temperature since the determination of the axial current density from the azimuthal magnetic field, Eq. (27), introduces a non-physical singularity on the symmetry axis [1].

It should be noticed that in the limit of a negligible radial current density compared to the axial current density, this formulation does not reduce to the quasi one-dimensional formulation of section 2.2.3. It reduces only to Eqs. (37) and (38), which are the same. In this limit it indeed defines B_{θ} from J_z , and at the same time J_z from B_{θ} . This implies that the quasi one-dimensional limit of the magnetic field formulation is not closed. Also, as detailed in section 2.2.2, the induction diffusion equation, Eq. (28), is derived from Eqs. (26)-(27), themselves derived from Gauss' law for magnetism and Ampère's law. The magnetic field formulation is thus a non-closed version of the axi-symmetric model since it does not account for the charge conservation equation. On the contrary, the electric potential formulation is closed, using the quasi one-dimensional closure relation, Eq. (38).

3 TEST CASES

Two test cases were investigated, see section 3.1 and 3.2, to study the influence of the two-dimensional phenomena in connection with the electromagnetic model. For this reason, the quasi one-dimensional approach of section 2.2.3 was not retained. The electromagnetic models used in these simulation tests are the remaining closed models:

- i) the three-dimensional approach,
- ii) the two-dimensional axi-symmetric approach with the formulation B1, and
- iii) the electric potential formulation.

The first test case, an infinite and electrically conducting rod, was retained since it has an analytic solution allowing testing the electromagnetic models. The second is the short arc (2 mm) of the water cooled GTAW test case described by Tsai and Kou [16]. It was investigated experimentally by Haddad and Farmer [15], and used in the literature as reference for testing arc heat source simulation models.

3.1 Infinite rod

The magnetic field induced in and around an infinite rod of radius r_o with constant electric conductivity, and constant current density J_z parallel to the rod axis, reduces to an azimuthal component B_θ . B_θ has the following analytic expression:

$$\begin{aligned} B_\theta(r) &= \frac{\mu_o J_z r}{2} \quad \text{if } r < r_o, \\ B_\theta(r) &= \frac{\mu_o J_z r_o^2}{2 r} \quad \text{if } r \geq r_o, \end{aligned} \quad (39)$$

where $J_z = I/(\pi r_o)$ denotes the current density along the rod axis, and I the current intensity.

A long rod of radius $r_o = 1$ mm with the large and uniform electric conductivity $\sigma_{rod} = 2700 A/(Vm)$, surrounded by a poor conducting region of radius $r_{ext} = 16$ mm, and uniform electric conductivity $\sigma_{sur} = 10^{-5} A/(Vm)$, was simulated. The conductivity σ_{rod} and σ_{sur} correspond to argon plasma at 10600 and 300 K, respectively.

The electric potential difference applied on the rod was set to 707 V, as indicated in Fig. 4, corresponding to a current intensity of 600 A. The electric potential gradient along the direction normal to the boundary was set to zero on all the other boundaries.

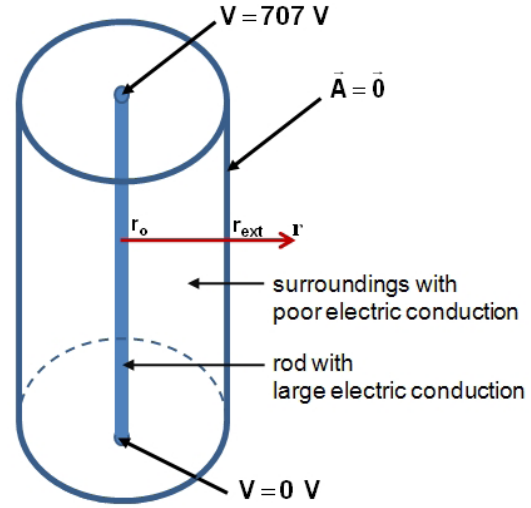


Figure 4: Schematic representation of the computational domain.

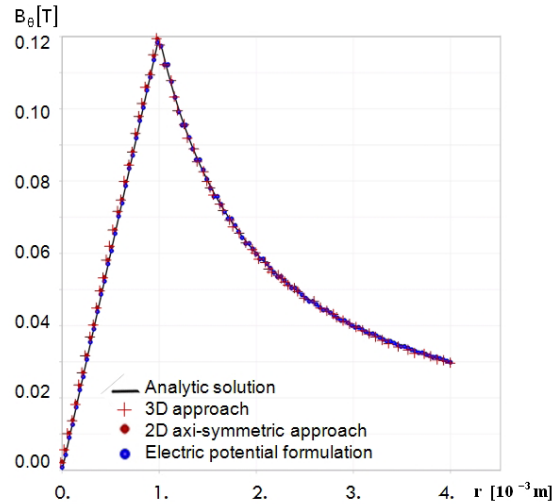


Figure 5: Angular component of the magnetic field along the radial direction ($r_o = 1 \times 10^{-3}$ m).

The magnetic field was calculated using i) the three-dimensional approach of section 2.2.1, ii) the two-dimensional and axi-symmetric approach B1 based on the magnetic potential, section 2.2.2, and iii) the electric potential formulation of section 2.2.4. In the three- and two-dimensional approaches, the magnetic potential \vec{A} was set to zero at $r = r_{ext}$, and its gradient

along the direction normal to the boundary was set to zero on all the other boundaries.

All the numerical simulations were done using the same mesh, so that they only differ in the expression used for calculating the magnetic field. The simulation results, plotted in Fig. 5 for the azimuthal component B_θ of the magnetic field, are all in perfect agreement with the analytic solution, as expected when the current density is aligned with the symmetry axis.

3.2 Water cooled GTAW with Ar shielding gas

The 2 mm long and 200 A argon arc studied by Tsai and Kou [16], based on the experimental measurements of Haddad and Farmer [15] reported in Fig. 6, is now considered.

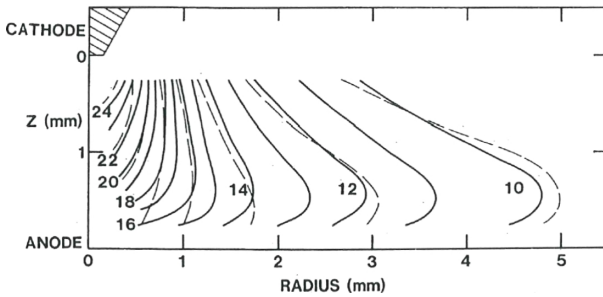


Figure 6: Temperature measurements of [15], courtesy of A.J.D. Farmer.

The configuration is sketched in Fig. 7. The electrode, of radius 1.6 mm, has a conical tip of angle 60° truncated at a tip radius of 0.5 mm. The electrode is mounted inside a ceramic nozzle of internal and external radius 5 mm and 8.2 mm, respectively. The pure argon shielding gas enters the nozzle at room temperature and at an average mass flow rate of $1.66 \times 10^{-4} \text{ m}^3/\text{s}$.

The temperature and the current density set on the cathode boundary are explicitly given [16]. The anode surface temperature was also set as proposed by Tsai and Kou [16], extrapolating the experimental results [15]. Looking at the experimental results, Fig. 6, it can be noticed that the measured temperature is rather difficult to extrapolate up to the anode. The boundary conditions set on the cathode also suffer from a lack of accuracy, as experimental measurements could not be done in the very close vicinity of the anode and cathode. These difficulties may explain the variety of

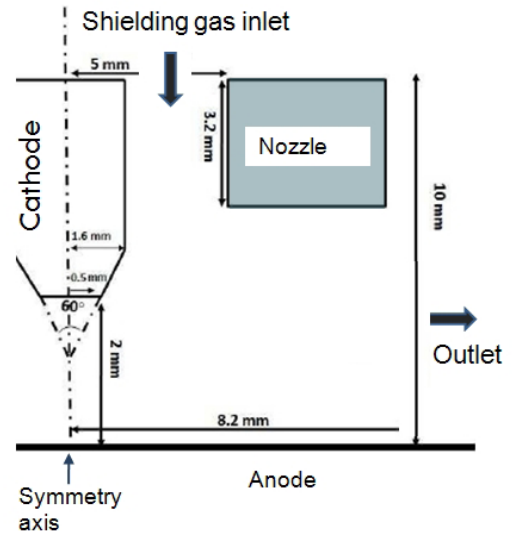


Figure 7: Schematic representation of the GTAW test case

boundary conditions used in the literature for simulating this test case.

The electromagnetic fields were calculated using i) the three-dimensional approach of section 2.2.1, ii) the two-dimensional and axi-symmetric approach B1 based on the magnetic potential, section 2.2.2, and iii) the electric potential formulation of section 2.2.4. Also, all the numerical simulations were done using the same mesh, so that they only differ in the expression used for calculating the magnetic field. The simulation results presented here were calculated using 25 uniform cells along the 0.5 mm tip radius, 100 uniform cells between the electrode and parent metal along the symmetry axis, and a total number of 136250 cells. A mesh sensitivity study has been done [22], concluding that the present mesh is sufficiently fine.

The numerical results from the i) three-dimensional approach and ii) two-dimensional axi-symmetric approach B1 are the same, which is expected as both approaches are based on the same physical assumptions. However, the results obtained with the electric potential formulation significantly differ, as shown in Fig. 8. Agreement is only observed at a distance below the cathode tip, where the radial component of the current density is negligible compared to the axial component (see Fig. 9). The electric potential formulation indeed defines B_θ neglecting the radial current

density component. The three-dimensional calculation, Fig. 9, shows that the radial component of the current density is not everywhere negligible, in particular next to the electrode tip, where the largest induced magnetic field is observed. So for the short arc studied here, neglecting the radial component of the current density results in a poor estimation of the magnetic pinch forces, and in turn of the arc velocity, as well as the pressure force the arc exerts on the base metal. Consequently, the electric potential formulation was not retained for simulating this short arc configuration.

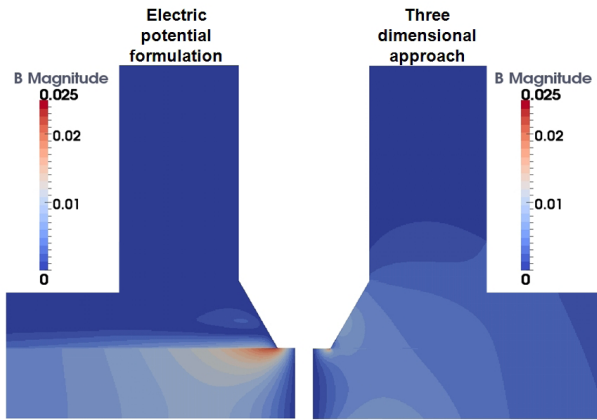


Figure 8: Magnetic field magnitude calculated with the electric potential formulation (left) and the three-dimensional approach (right).

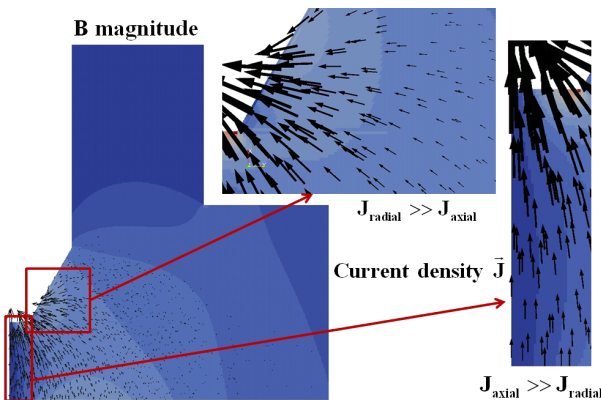


Figure 9: Current density vector calculated with the three-dimensional approach.

The next simulation results were all obtained with the three-dimensional approach, which is here more natural to use as OpenFOAM is a three-dimensional simulation software. Notice that the radial direction is now denoted y instead of r , and the axial direction x instead of z .

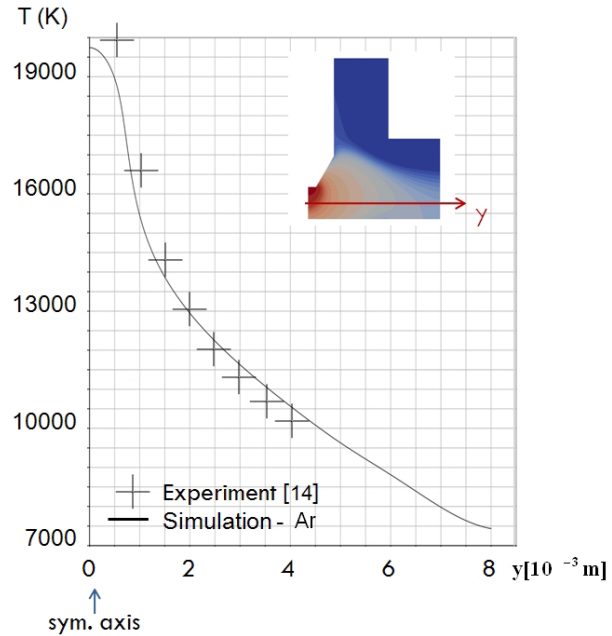


Figure 10: Temperature along the radial direction, 1 mm above the anode.

The calculated temperature is plotted along the radial direction 1 mm above the anode in Fig. 10, and along the symmetry axis in Fig. 11 (solid line). The experimental data [15], shown in Fig. 6, are used for comparison with the numerical results along the radial direction, in Fig. 10. A good agreement is obtained. The comparison along the symmetry axis is difficult to perform, as the isotherms represented in Fig. 6 are not plotted in this area. We can however observe that the maximum temperature obtained numerically seems to underestimate the experimental one by about 10%. This could be due to the boundary conditions set on the anode and cathode. Other boundary conditions also used in the literature are investigated in section 3.4.

The test cases of the next section were investigated as a preliminary study for future extension of the model

to active gas welding. They should be considered as academic, for various reasons detailed below.

3.3 Ar- $x\%$ CO₂ shielding gas

Plasma arc simulations for the test case of section 3.2 were also done changing the shielding gas composition to Ar- $x\%$ CO₂, and the four following cases: pure argon ($x=0$), pure carbon dioxide ($x=100$), and mixtures of these two gases with $x=1\%$ and 10% in mole. In each case the thermodynamic and transport properties were tabulated as function of the temperature up to 30 000K. The tables were implemented in OpenFOAM-1.6.x as described in section 2.1. For pure argon and pure carbon dioxide the data tables result from derivations done by Rat *et al.* [20] and André *et al.* [21] using kinetic theory. For the other mixtures (with $0 < x < 1$) the data tables were prepared doing an additional calculation step, based on the data for pure argon, pure carbon dioxide, and standard mixing laws. The mixing laws for calculating the specific heat and the enthalpy of a mixture use mass concentration as weighting factor [23]. When applied to the calculation of the viscosity, the thermal conductivity and the electric conductivity of a mixture, the molar concentration is instead used as weighting factor [24].

Because of lack of experimental data, the boundary conditions set on the electrode and the base metal are the same as in section 3.2. These approximate boundary conditions are most probably too rough when the shielding gas contains a significant amount of CO₂. Also, the difficulty met in setting appropriate boundary conditions on the anode and cathode raises the future need of extending the simulation model coupling cathode and anode simulation to the thermal plasma arc.

The shielding gas containing $x=1\%$ in mole of CO₂ should be close to the maximum amount of CO₂ allowing producing a stable electric arc with a tungsten electrode and water cooled base metal. Experiments are being prepared for characterizing this case. For a larger amount of CO₂ in the shielding gas, significant electrode oxidation is expected, leading to arc instability. A solution for making experiments feasible with a tungsten electrode could consist in shielding locally the electrode tip with an inert gas such as argon. Such a local shielding is not included in the present simulations.

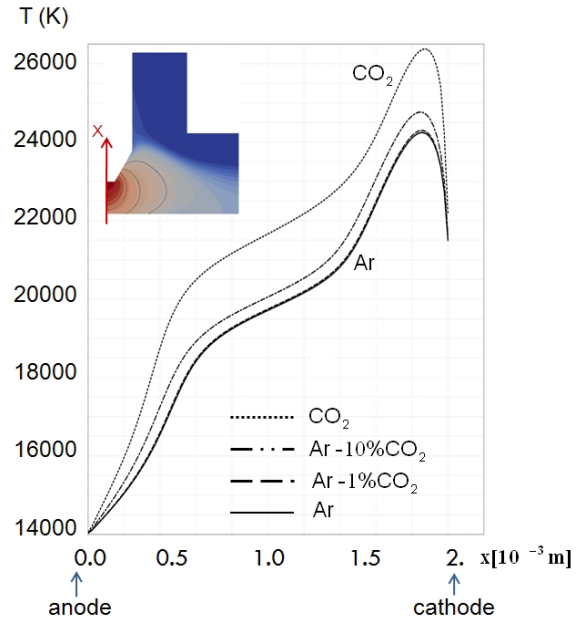


Figure 11: Temperature along the symmetry axis.

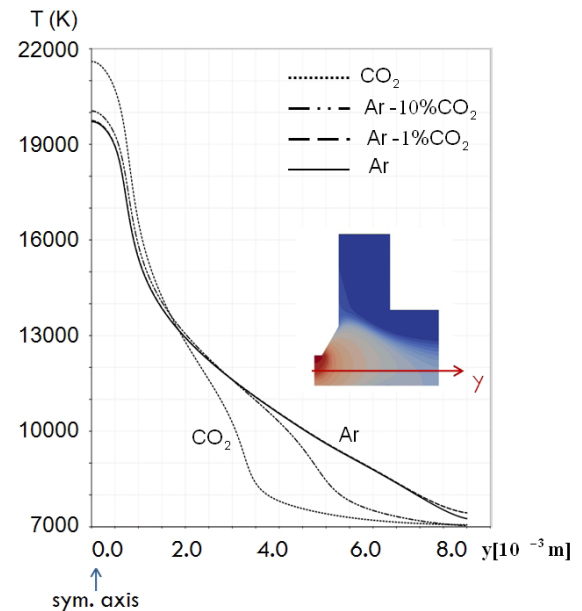


Figure 12: Temperature along the radial direction, 1 mm above the anode.

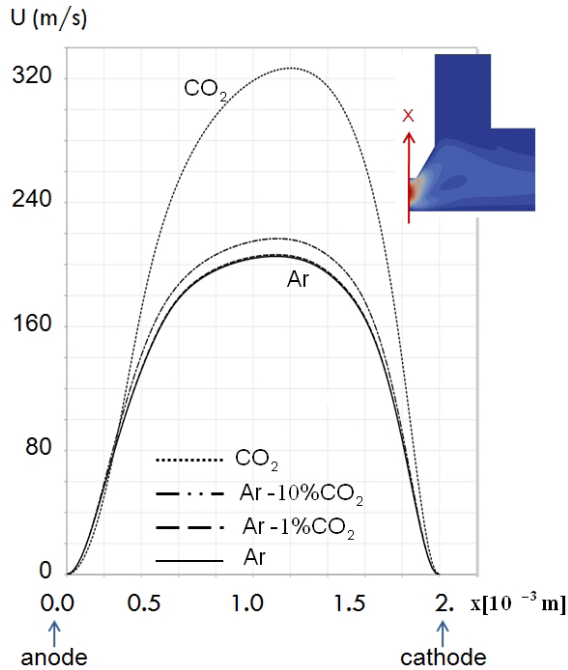


Figure 13: Velocity along the symmetry axis.

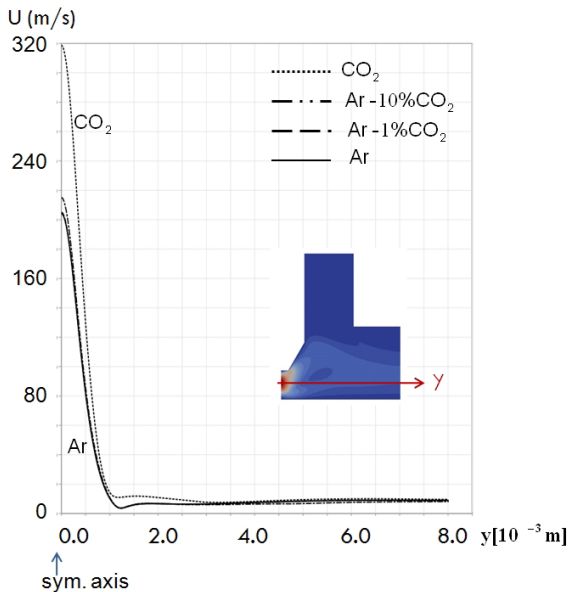


Figure 14: Velocity along the radial direction, 1 mm above the anode.

The present aim is to evaluate qualitatively the influence of the amount of active gas on the plasma arc temperature and velocity for given boundary conditions. The calculated temperature is plotted along the symmetry axis in Fig. 11, and along the radial direction 1 mm above the anode in Fig. 12. In a similar way, the calculated velocity is plotted along the symmetry axis in Fig. 13, and along the radial direction 1 mm above the anode in Fig. 14.

The simulation results clearly show that the presence of carbon dioxide results in an increased arc temperature (Figs. 11, 12), and a constriction of the temperature field above the base metal (Fig. 12). It also results in a significant increase of the plasma arc velocity (Figs. 13, 14), which in turn increases the pressure force applied on the base metal, but no significant change concerning the extent of the plasma jet just above the base metal (Fig. 14).

3.4 Boundary conditions

As underlined above, the available experimental measurements need to be extrapolated for estimating a priori the boundary conditions. The extrapolation is somewhat uncertain, which may explain the variety of boundary conditions used in the literature.

Three test cases (a, b, and c) that differ only by the boundary conditions set on the electrode and the anode were calculated to evaluate the influence of these boundary conditions on the plasma arc. In case a (treated above using the boundary conditions defined by Tsai and Kou [16]), the current density is uniform on the 0.5 mm radius cathode tip, and it decreases linearly down to zero as the radius tip increases. In case b all the current density (also uniform) goes through the 0.5 mm radius cathode tip. The boundary conditions on the anode are the same in case a and b. In case c the boundary conditions on the cathode are the same as in case b. Case c is associated with an extreme thermal condition on the anode for testing the model: its anode does not conduct heat. In all cases, argon is used as shielding gas.

The temperature and the velocity calculated for each case are plotted along the symmetry axis in Fig. 15 and Fig. 16, respectively. The pressure on the base metal is plotted in Fig. 17. It can be observed in Fig. 15 that there is a large influence of the cathode current density distribution on the cathode on the maxi-

imum arc temperature. Also, compared to case a, the maximum temperature of case b is much closer to the maximum temperature observed experimentally. The thermal boundary condition on the anode has almost no influence on the maximum arc temperature. However, it can significantly affect the heat transferred to the anode base metal, as it significantly changes the temperature close to the anode.

Finally, Fig. 16 and 17 show that the velocity along the symmetry axis and the pressure force on the base metal are significantly changed for each variation tested on the anode and cathode boundary conditions.

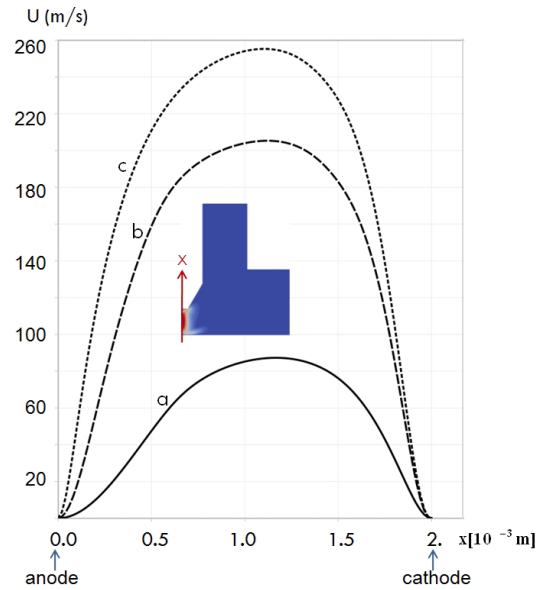


Figure 16: Influence of the anode and cathode boundary conditions on the velocity along the symmetry axis.

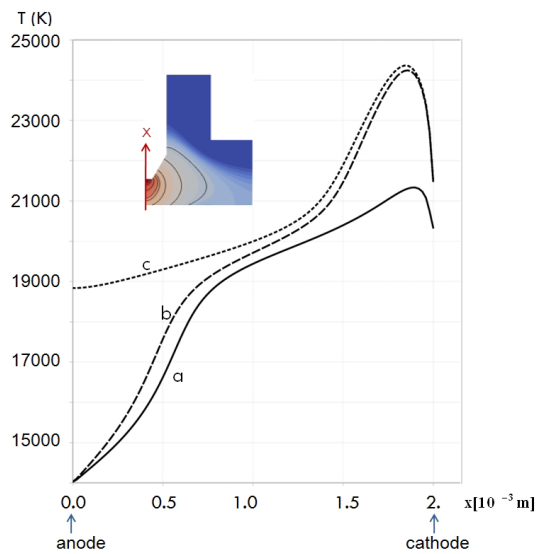


Figure 15: Influence of the anode and cathode boundary conditions on the temperature along the symmetry axis.

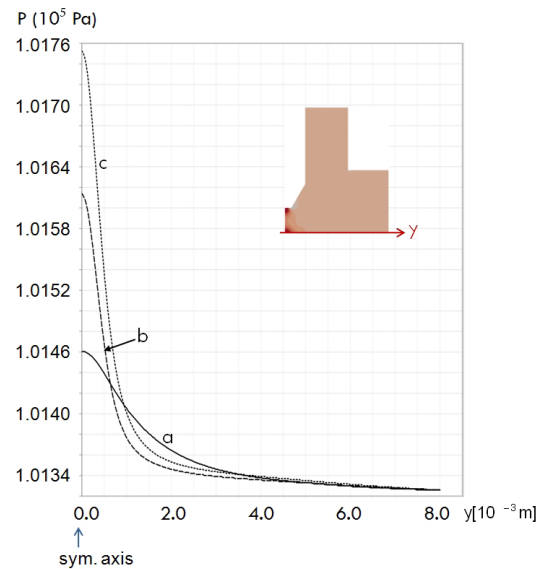


Figure 17: Influence of the anode and cathode boundary conditions on the pressure on the base metal.

4 CONCLUSION

This study focused on the modeling and simulation of an electric arc heat source, coupling thermal fluid mechanics with electromagnetics. The model, valid for the plasma core, was implemented in the open source software OpenFOAM. Different approaches were considered for modeling the electromagnetic fields:

- i) the three-dimensional approach,
- ii) the two-dimensional axi-symmetric approach,
- iii) the electric potential formulation, and
- iv) the magnetic field formulation as described by Ramírez *et al.* [1].

Models i) to iii) reduce to the same quasi one-dimensional limit for an axi-symmetric configuration with negligible radial current density, contrary to model iv). Model iv) is a non-closed version of the axi-symmetric model. It does not account for the charge conservation equation. On the contrary, the electric potential formulation is closed with a quasi one-dimensional closure relation. Models ii) to iv) cannot represent the same physics when the radial current density is significant, such as for a short arc or an electrode tip with a conical shape.

The electromagnetic solver was tested against the analytic solution of an infinite electric rod using models i) to iii). The solutions are in perfect agreement.

The coupled solver was tested against experimental measurements for GTAW with argon shielding gas and a short arc (2 mm). The numerical solution for the azimuthal component of the magnetic field then significantly differs when applying the electric potential formulation iii). This approach indeed neglects the radial current density component. For axi-symmetric configurations with non-negligible radial effects, such as short arcs, this simplification is not everywhere justified. The numerical results obtained using models i) and ii) show a good agreement with the experimental data when such comparisons can be made.

Difficulty were met in setting appropriate boundary conditions, either because of lack of experimental data, or because of a too large freedom for extrapolating available experimental data up to the anode and cathode surface. In addition different possible conditions significantly affect the simulation results, such as the plasma arc temperature and velocity. The temperature and current density distribution on the elec-

trode surface should thus be calculated rather than set, to enhance the predictive capability of the simulation model. The solution of the temperature and electromagnetic fields inside the anode and cathode, and the modeling of the plasma arc sheath doing the coupling with the plasma core, will thus be included in the forthcoming development of the simulation model.

Acknowledgment: The authors thank Prof. Jacques Aubreton and Prof. Marie-Françoise Elchinger for the data tables of thermodynamic and transport properties they did provide. This work was supported by KK-foundation in collaboration with ESAB, Volvo Construction Equipment and SSAB. Håkan Nilsson was in this work financed by the Sustainable Production Initiative and the Production Area of Advance at Chalmers. These supports are gratefully acknowledged.

Grateful acknowledgement is made to the Welding Journal for permission to reproduce figure 5 from the paper "Temperature Measurements in Gas Tungsten Arcs" (1985, 64(12)).

5 References

- [1] M.A. Ramírez , G. Trapaga and J. McKelliget (2003). A comparison between two different numerical formulations of welding arc simulation. *Modelling Simul. Mater. Sci. Eng.*, **11**, pp. 675-695.
- [2] L. Lindgren, B. Babu, C. Charles, and D. Wedberg (2010). Simulation of manufacturing chains and use of coupled microstructure and constitutive models. *Finite Plasticity and Visco-plasticity of Conventional and Emerging Materials*, Khan, A. S. and B. Farrokh, (red.). NEAT PRESS, 4 s.
- [3] A. Kumar, and T. DebRoy (2007). Heat transfer and fluid flow during Gas-Metal-Arc fillet welding for various joint configurations and welding positions. *The minerals, metals and materials society and ASM International*.
- [4] K.C. Hsu, K. Etemadi and E. Pfender (1983). Study of the free-burning high intensity argon arc, *J. Appl. Phys.*, **54**, pp. 1293-1301.
- [5] Y. Tanaka, T. Michishita and Y. Uesugi (2005). Hydrodynamic chemical non-equilibrium model

- of a pulsed arc discharge in dry air at atmospheric pressure. *Plasma Sources Sci. Technol.* **14**, pp. 134-151
- [6] K. Yamamoto, M. Tanaka, S. Tashiro, K. Nakata, K. Yamazaki, E. Yamamoto, K. Suzuki, and A.B. Murphy (2008). Numerical simulation of metal vapor behavior in arc plasma. *Surface and Coatings Technology*, **202**, pp. 5302-5305.
- [7] J. Wendelstorf (2000). Ab initio modelling of thermal plasma gas discharges (electric arcs). PhD. Thesis, Carolo-Wilhelmina University, Germany.
- [8] M. Tanaka, H. Terasaki, M. Ushio and J. J. Lowke (2002). A unified numerical modeling of stationary tungsten-inert-gas welding process. *Metall. and Mater. Trans. A*, **33A**, pp.2043-2052
- [9] J. Hu, and L.S. Tsai (2007). Heat and mass transfer in gas metal arc welding. Part I: The arc, Part II: The metal. *International Journal of Heat and Mass Transfer* **50**, pp. 808-820, 833-846.
- [10] G. Xu, J. Hu and H.L. Tsai (2009). Three-dimensional modeling of arc plasma and metal transfer in gas metal arc welding. *International Journal of Heat and Mass Transfer*, **52**, pp. 1709-1724.
- [11] J. J. Gonzalez, F. Lago, M. Masquère, and X. Franceries (2005). Numerical modelling of an electric arc and its interaction with the anode: Part II. The three-dimensional model - influence of external forces on the arc column, *J. Phys. D: Appl. Phys.*, **36**, pp. 306-318.
- [12] F. Lago, J. J. Gonzalez, P. Freton, and A. Gleizes (2004). A numerical modelling of an electric arc and its interaction with the anode: Part I. The 3D model, *J. Phys. D: Appl. Phys.*, **37**, pp. 883-897.
- [13] R. Bini, M. Monno, and M.I. Bolos (2006). Numerical and experimental study of transferred arcs in argon. *J. Phys. D: Appl. Phys.*, **39**, pp. 3253-326
- [14] J. McKelliget, and J. Szekely (1986). Heat transfer and fluid flow in the welding arc, *Metall. Mater. Trans A*, **17**, pp. 1139-1148.
- [15] G.N. Haddad, and A.J.D. Farmer (1985) Temperature measurements in gas tungsten Arcs. *Welding Journal* **24**, pp. 339-342.
- [16] M.C.Tsai, and Sindo Kou (1990). Heat transfer and fluid flow in welding arcs produced by sharpened and flat electrodes. *Int J. Heat Mass Transfer*, **33**, 10, pp. 2089-2098.
- [17] M. Sass-Tisovskaya (2009). *Plasma arc welding simulation with OpenFOAM*, Licentiate Thesis, Chalmers University of Technology, Gothenburg, Sweden.
- [18] I. Choquet, and B. Lucquin-Desreux (2011), Non equilibrium ionization in magnetized two-temperature thermal plasma, *Kinetic and Related Models*, **4**, 3, pp. 669-700.
- [19] C. Delalondre (1990), Modélisation aérodynamique d'arcs électriques à forte intensité avec prise en compte du déséquilibre thermodynamique local et du transfert thermique à la cathode, PhD. Thesis, Rouen University, France.
- [20] V. Rat, A. Pascal, J. Aubreton, M.F. Elchinger, P. Fauchais and A. Lefort (2001). Transport properties in a two-temperature plasma: theory and application. *Physical Review E*, **64**, 026409.
- [21] P. André, J. Aubreton, S. Clain, M. Dudeck, E. Duffour, M. F. Elchinger, B. Izrar, D. Rochette, R. Touzani, and D. Vacher (2010), Transport coefficients in thermal plasma. Applications to Mars and Titan atmospheres, *European Physical Journal D* **57**, **2**, pp. 227-234.
- [22] I. Choquet, H. Nilsson, and M. Sass-Tisovskaya (2011). Modeling and simulation of a heat source in electric welding, *In Proc. Swedish Production Symposium, SPS11*, May 3-5, 2011, Lund, Sweden, pp. 202-211.
- [23] R.E. Sonntag, C. Borgnakke, and G.J. Van Wylen (2003). *Fundamentals of thermodynamics*, Wiley, 6th edition.
- [24] R. J. Kee, M. E. Coltrin, P. Glaborg (2003). *Chemically reacting flow. Theory and Practice*, Wiley Interscience.